Hydriding kinetics of Mg—TiH$_2$ fine dispersions obtained by mechanosynthesis

A. Biasetti *, M. Meyer, L. Mendoza Zélis

Institute of Physics La Plata-CONICET, College of Exact Sciences—National University of La Plata, 49 and 115, 1900, La Plata, Argentina

ARTICLE INFO

ABSTRACT

Mg80—Ti20 hydride systems were prepared via reactive ball milling following two different procedures: grinding Mg with Ti or TiH2, in both cases under H2 atmosphere. Such systems were subjected to several cycles of hydrogen uptake and release in volumetric Sieverts apparatus under different pressure and temperature conditions. A structural characterization from SEM images and XRD patterns reveals no essential microstructural differences between the samples obtained by different routes, although a growth in domain size with temperature is observed. Also, the slowing of the kinetics when the temperature goes down is more pronounced in the specimen fabricated by the second route.

The influence of the transformed and untransformed phase fractions on the absorption kinetics can be well described using a double Hill function. Such complex function takes into account two distinguishable processes, with and without nucleation, that differentiate themselves as temperature increases. The first one may be related to surface absorption and the second tentatively ascribed to reactions at grain boundaries, dislocations and other extended defects.

The fitted values may then be associated to physical constants of the processes occurring during hydrogen absorption in both regions.

1. Introduction

Solid hydrides are thought to be of crucial importance as hydrogen storage materials in global energy prospects based on hydrogen as an energy carrier. While Mg is nominally a good candidate for solid-state hydrogen storage, due to its capacity (up to 7.6 wt% H), availability and low cost, its sorption kinetics should be considerably improved for it to become of practical use in reliable applications. The reduction of grain sizes to the nanometer scale has demonstrated to be useful for reducing hydrogen uptake/release times [1,2]. Furthermore, the addition of small quantities of transition metals has been used with the objective of destabilizing the hydride. Kinetic properties can be significantly improved by combining a nanometric microstructure and the addition of metals. Particle size reduction shortens the length of the diffusion path for H atoms and produces a high surface density for H chemisorption. Additives such as transition metals facilitate H chemisorption and promote the dissociation of the H molecule. For example, sorption kinetics has been highly enhanced by milling Mg with several transition metals such as Nb [3,4,5], V [4,6], Pd [7] and Ni [8].

The Mg——Ti system is immiscible, so metastable alloys and hydrides can be produced either in thin film [9,10] by vapor deposition or bulk geometries [11,12] via ball milling among others. These metastable phases constitute a promising route to destabilize magnesium hydride. Anastasopol et al. [13] reported a reduction in the formation enthalpy (-45 KJ/mol H$_2$) and entropy (-84 J/Kmol H$_2$) of hydrogenation of MgTi alloys made by spark discharge, but the thermal stability upon cycling is problematic, affecting their potential use for hydrogen storage. On the other hand, good cycling and kinetic results have been obtained in the MgH$_2$—TiH$_2$ system synthesized by reactive ball milling [14–17].

Ponthieu et al. [18] studied the Mg——Ti system, in particular Mg$_{0.7}$Ti$_{0.3}$, and concluded that it can store reversibly up to 3.7 wt% at 573 K without changes up to 100 cycles.

In previous work [19], we studied the formation kinetics and microstructure of Mg——Ti hydrides produced via reactive ball milling following two different routes. We found that alloying Mg with Ti or TiH$_2$ leads to very fine Mg——Ti dispersions with good hydrogenation properties without significant reduction in their hydrogen gravimetric capacity [20,21]. Indeed, the need for a hydrogen gravimetric density up to 6% [22] is well satisfied for Mg$_x$Ti$_{(1-x)}$ systems with x ≥ 0.7.

In the present work, we focus our attention on the study of the absorption kinetic properties in some of the samples fabricated via reactive ball milling. The 80:20 ratio was found to be satisfactory, accounting for the hydrogen wt% required with good formation kinetics [19].

* Corresponding author.
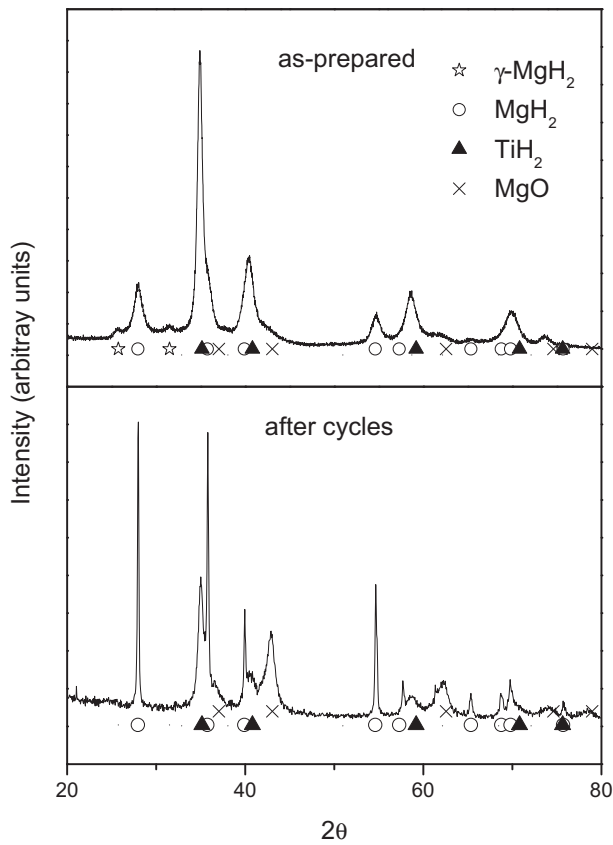*E-mail address:* biasetti@fisica.unlp.edu.ar (A. Biasetti).

Fig. 1. Powder diffraction patterns for as prepared and after cycles specimens. Also are shown the peak positions for the main phases observed.

In studying the kinetics, different approaches have been employed to identify the processes involved, among them, the search for a *rate-limiting step* and the identification of *nucleation and growth processes* [23–27]. In the present work, a composite function with two additives

Hill functions [28]:

$$\chi(t) = \chi_1 \frac{t^{n_1}}{\tau_1{}^{n_1} + t^{n_1}} + \chi_2 \frac{t^{n_2}}{\tau_2{}^{n_2} + t^{n_2}} \tag{1}$$

is necessary to consistently fit the whole set of measured absorption curves. An interpretation in terms of two different regions, with distinct absorption behavior, is thus suggested.

2. Experimental

Mixtures of Mg——Ti in atomic ratio 80:20 were obtained from Mg granules and Ti powder of purity 99.9% and 99.4%, respectively. The mixtures were placed in a cylindrical steel milling vial together with one steel ball (ø = 12 mm) and ground in an oscillatory ball mill in H_2 atmosphere (route *a*). A second group of samples was prepared from a mixture of Mg and TiH_2 (obtained also by mechanosynthesis), which was ground in H_2 atmosphere (route *b*). The details of the milling procedure and the resulting *formation* kinetics were described previously [19].

Sieverts type apparatus [29,30] was used to carry out several dehydriding and hydriding cycles on the studied systems as well as many thermal treatments. Specimens of 100–200 mg were extracted from the as-prepared powders and placed in the reactor, which consists of a stainless steel cylinder of about 0.6 cm³. A quartz wool filter was used at the extremes of the reactor, avoiding powder spreading outside the reactor. Temperature was measured with a PT 100 sensor in contact with the sample, inside the reactor. On the other hand, the instantaneous pressure P as a function of time was measured with a gauge transducer sensor. A configuration of manual and automatic valves was designed in order to perform different experiments controlling the initial pressure for absorptions and minimize the valve operation times. A standard known volume was used to determine the effective reactor volume at the working temperature.

Basically, two kinds of experiments were carried out. On the one hand, hydrogen desorption–absorption experiments at constant volume: first heating the sample from an uptake state at RT, and then cooling it again. Specifically, the temperature was increased up to
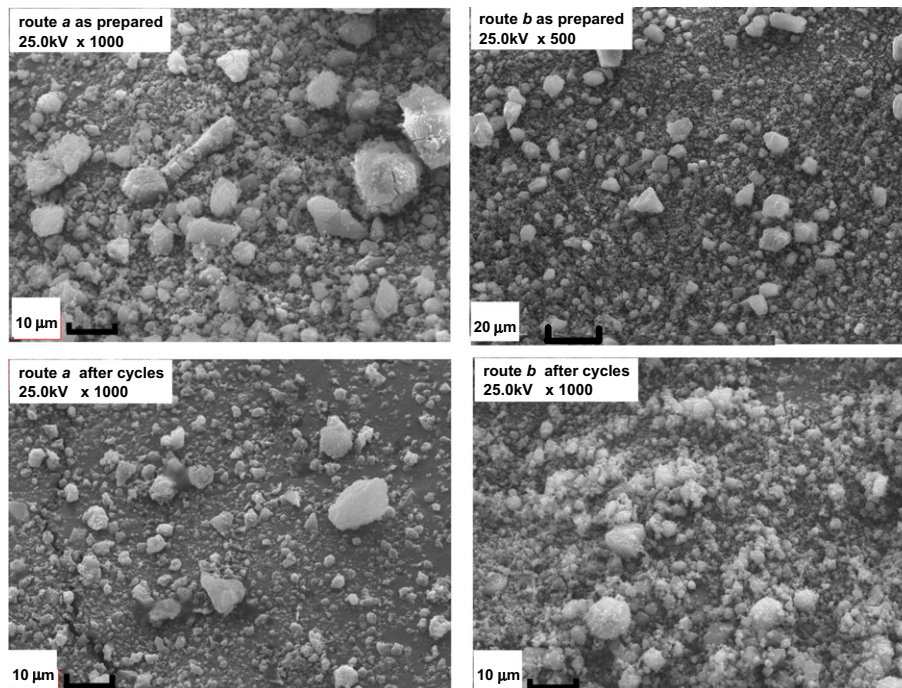

Fig. 2. SEM images for samples prepared through routes *a* and *b*, as prepared and after cycles.

380 °C at a heating rate of 10 K/min and then, the oven was turned off, while P-T curves in which desorption and absorption processes are well identified were obtained [31]. From them, equilibrium pressure–temperature curves were built. On the other hand, we carried out hydrogen desorption-absorption experiments at constant T. Specifically for absorption from a discharged state, at an initial pressure below 0.3 bar and a defined T, one valve connecting the reservoir chamber and the reactor was opened and closed automatically, injecting gas into the reactor from the reservoir compartment. From this value, the reactor pressure starts decreasing due to a change in the number of moles (absorption process) of gas according to $\Delta\chi_{H_2} = \frac{\Delta PV}{RT}$. The pressure as a function of time was recorded till the change in the pressure value fell below the signal noise during a fixed time, which was long enough to consider that further sorption was negligible. In desorption experiments, from an initial uptake state, at defined T and pressure above the equilibrium pressure, the same valve was opened-closed automatically, but now evacuating H_2 gas and, in the same way as before, the increment of pressure in the reactor due to desorption was recorded as a function of time.

X-ray diffraction patterns were obtained with a Philips PW1710 and PW1732/10 diffractometers, both using CuKα radiation in Bragg geometry in the 2θ range: 20° to 80°, with steps of 0.05°. For selected samples, a step of 0.02° was used to improve the statistics in order to perform a Rietveld refinement.

SEM images were recorded using a Philips SEM 505 microscope at several magnifications from 500× to 1000×. Also, composition maps and analysis were obtained using the EDAX microprobe.

3. Results

3.1. Microstructures

X-ray diffraction patterns were obtained both for the as-prepared ground mixtures by routes *a* and *b*, and the same specimens after thermal treatments.

In the diffraction patterns for both fabrication routes, γ-MgH_2 (metastable), rutile-MgH_2 and δ-TiH_2 phases were identified. A small proportion of MgO was also identified, probably due to the unavoidable oxidation occurring during XRD measurements performed at open atmosphere. The XRD powder patterns are displayed in Fig. 1, which shows a change in the cell dimensions of the TiH_2 phase for milling
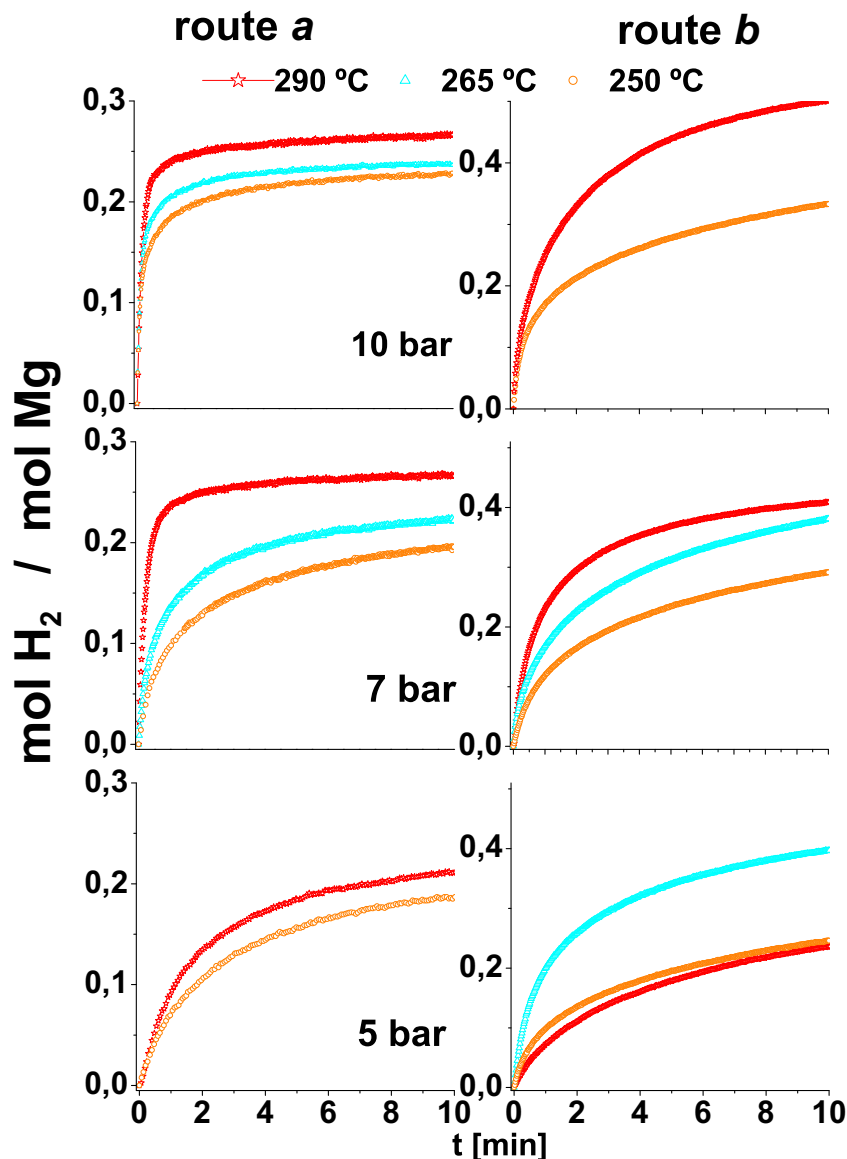

Fig. 3. Kinetics absorption curves for samples fabricated through routes *a* (left) and *b* (right) for different pressures and varying temperature.

route *a*, probably due to substitutional Mg. Rietveld analysis was performed in order to estimate the mean crystallite size and to refine lattice parameters.

The SEM images corresponding to the as-prepared mixtures and those for the same ones after thermal treatments are shown in Fig. 2. Some particles above 40–50 μm were founded, but most of them are below 20 μm diameter.

Representative images were chosen to illustrate the heterogeneous size particle distribution. Composition maps reveal a fine microstructural dispersion of Mg and Ti in the as-prepared specimens as well as in the thermally treated ones.

3.2. Kinetic curves

Absorption kinetic curves of the samples obtained by routes *a* and *b*, at different initial pressures and different temperatures, are shown in Figs. 3 to 5. It has to be mentioned that our specimens are able to absorb hydrogen from 240 °C at pressures from 3 bar.

Similarly, some desorption kinetic curves comparing both routes at different temperatures are depicted in Fig. 6.

The progress of the absorption (desorption) reaction in the reactor was represented by the instantaneous number of hydrogen atoms incorporated into the mixture relative to the number of reactive metallic atoms

$$\chi(t) = \frac{N_{H_2}(t)}{N_{Mg}}$$

where $N_{H_2}(t)$: number of H_2 moles absorbed (desorbed) at a time t, and N_{Mg}: number of Mg moles of the specimen.

4. Analysis and discussion

From the XRD patterns we could identify the phases present before and after the specimens were subjected to thermal treatments. It must to be noticed that the γ-MgH$_2$ metastable phase disappeared after the first thermal cycle. Since XRD measurements were performed at open atmosphere, a partial oxidation of the specimens after they were removed from the Sieverts reactor was unavoidable. The XRD patterns of the ground samples prepared through the two different routes were very similar as regards the phases present.

On the other hand, Rietveld refinements of the patterns were performed to characterize the crystal structure and estimate the grain size. The XRD pattern refinements of a ground specimen and
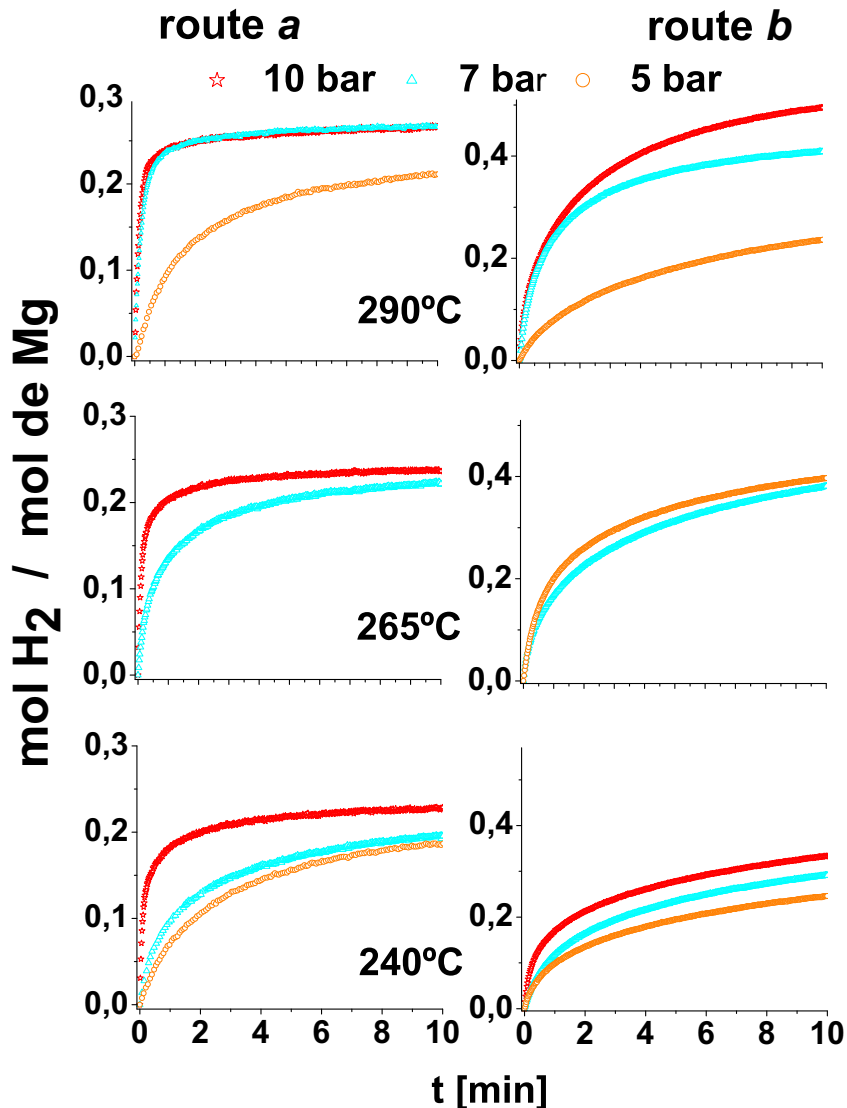

Fig. 4. Kinetics absorption curves for samples fabricated through routes *a* (left) and *b* (right) for different temperatures and varying pressure.
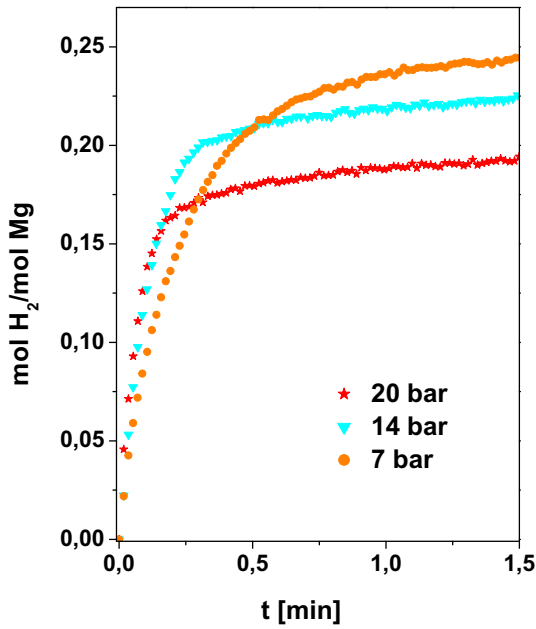
Fig. 5. Kinetics absorption curves for samples fabricated through route *a* for 290 °C at different pressures.

of a thermally treated one are shown in Fig. 7. FullProf software was used to make the refinements [32]. Table I lists the refined lattice parameters and the estimated mean grain sizes from such refinements.

The mean grain size of thermally treated samples increased. We then performed a single experiment of the first type described above and analyzed the sample by XRD. The respective pattern revealed that a single absorption/desorption cycle was enough to produce the grain growth observed.

According to microscopy images, both fabrication routes lead to fine homogeneous dispersion of the constituents and a broad distribution of particle size and shape. MgH$_2$ particle sizes are below 50 μm in diameter, which assures complete hydrogenation after the absorption
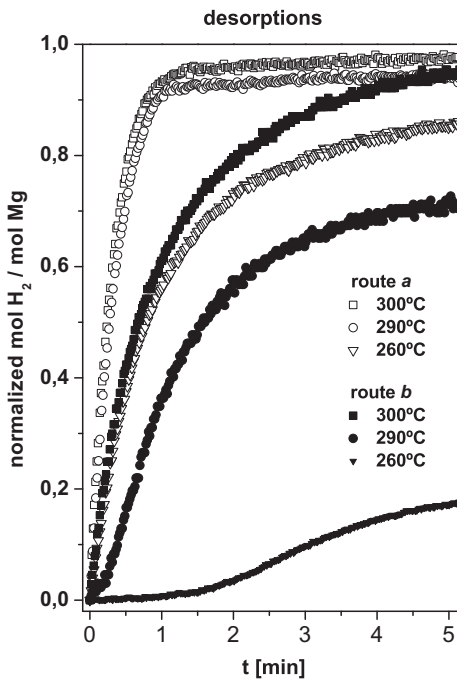

Fig. 6. Kinetics normalized desorption curves for samples fabricated through routes *a* (unfilled symbols) and *b* (filled symbols) for different temperatures.
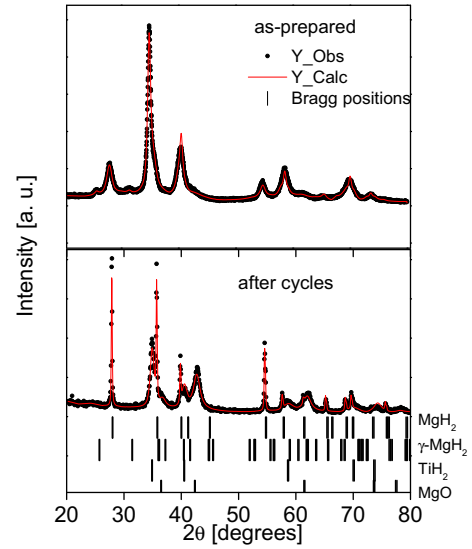

Fig. 7. Rietveld refinement of the powder diffraction patterns. The narrowing of MgH$_2$ peaks is evident.

processes in the volumetric equipment, as was experimentally established [33–38].

Compositional analysis by EDAX showed that the Mg:Ti ratio was kept near 80:20 through all the observed particles in all the studied samples.

The MgH$_2$—TiH$_2$ systems result in a heterogeneous fine dispersion powder.

In summary, as revealed by SEM and XRD, structural characteristics do not show significant differences between the two sets of samples; however, the powders fabricated by different routes exhibit different kinetics and also different capability of holding the reversibility observed at the first sorption cycle.

From this, we should say that the simultaneous formation reactions of MgH$_2$ and TiH$_2$ related to route *a*, leads to a configurational nanostructure different form that of route *b*, in which TiH$_2$ is already formed This should mean that a different sort of defects and different configurations at nanostructure scale probably should be the responsible of such behaviors.

4.1. Modeling kinetic curves

A great number of hydrogen absorption/desorption cycles were carried out for the samples prepared through routes *a* and *b*. Emphasis was put on comparing the kinetics for different pressures, temperatures and fabrication routes. These dependences are displayed in Figs. 3 to 5.

As can be seen in Fig. 3, route *a* has better kinetics than route *b*, but a decrease of capacity is noted. At the lower pressures, temperature affects more markedly the kinetic corresponding to route *b*. At pressures around 10 bar, temperature changes mainly affect the capacity rather

Table I
Rietveld refined cell parameters and averages crystallite size and strain.

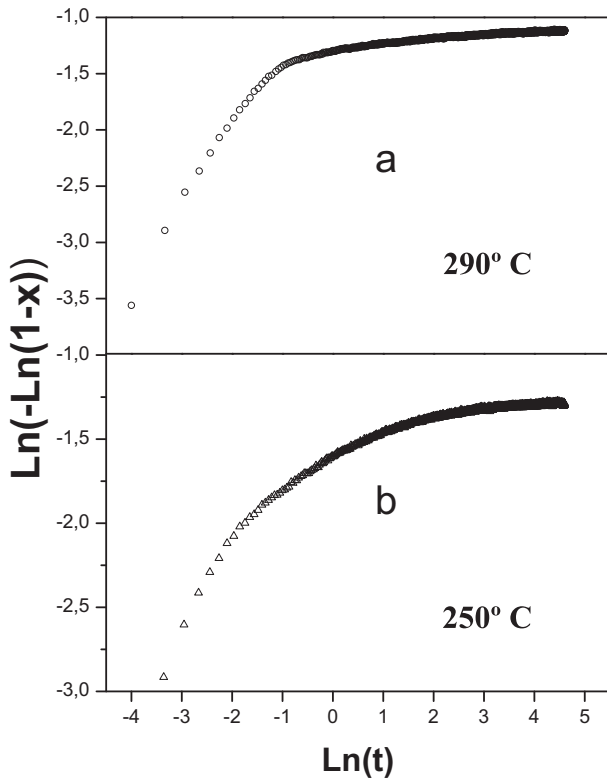| Fabrication route	Phase	Cell parameters [Å]	Crystallite size [nm]	Strain [×10^{-4}]
a (As-prepared)	$\beta-$MgH$_2$	a: 4.5064 c: 3.0260	10	120
	$\gamma-$MgH$_2$	a: 4.8544 b: 4.8991 c: 4.9900		
	$\delta-$TiH$_2$	a:4.4541		
	MgO	a:4.4112		
b (after cycles)	$\beta-$MgH$_2$	a: 4.5217 c: 3.0226	350	~0
	$\delta-$TiH$_2$	a: 4.4478		
	MgO	a: 4.2300		

Fig. 8. Typical Avrami plot obtained for kinetics at temperatures a) 290°C, b) 250°C.

than the kinetic properties for route *a*. However, in the case of route *b*, both the kinetic and capacity are affected by the change of temperature. This can also be observed in Fig. 4, where the kinetic values are ordered as a function of temperature.
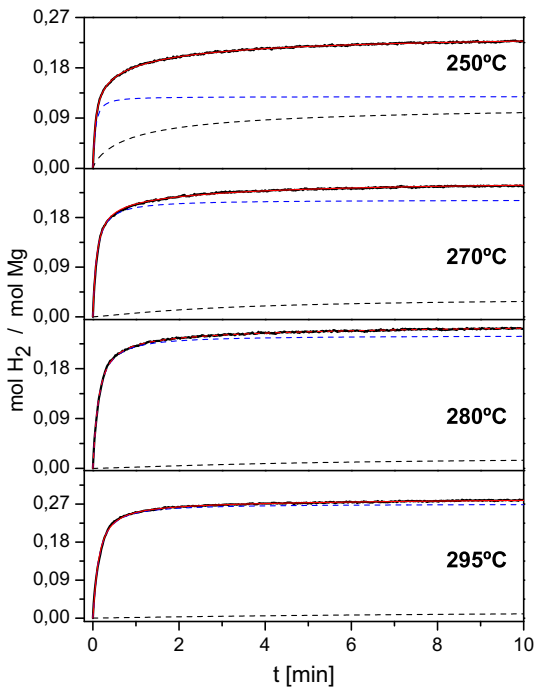

Fig. 9. Fits for the kinetic absorption curves of samples prepared through route a. The two components of the fitted doubly hill function, are represented by dotted curves and the fit by a red line.
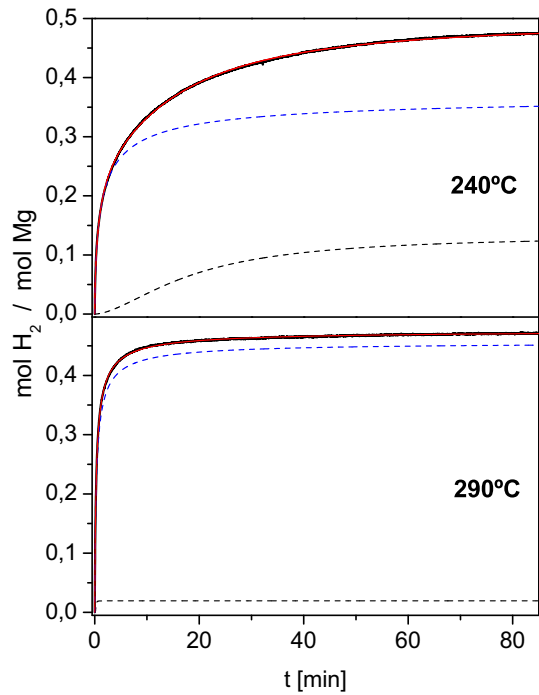

Fig. 10. Fits for the kinetic absorption curves of samples prepared through route b are represented by dotted curves and the fit by a red line.

In Fig. 5, kinetic absorption curves at 290 K and different pressures are compared in order to show the compromise between kinetic properties and capacity related to the initial pressure P_i. When the pressure increases from 7 to 20 bar, although the kinetics is faster, there is a reduction in capacity, as observed by H.-Y. Tien et al. [39]. When the pressure is high, a great number of nuclei of the hydride phase emerge at the beginning and start to grow quickly, probably covering all the particle surfaces, then damping the subsequent hydriding of the core. However, at lower pressures there are fewer quantities of initial nuclei that grow up without covering the entire surface. This allows the diffusion of hydrogen towards the inside of the core.

Characteristic Avrami plots corresponding to high and low temperature absorption processes are shown in Fig. 8. For high temperatures, the plot exhibits two defined straight regions associated with well-defined kinetic regimes. On the other hand, for low temperatures it is hard to determine a finite number of regions and instead, a continuous variation is found.

Due to such limitations we tested a model to describe the kinetics as a function of the transformed and untransformed phases.

The influence on the sorption reaction rate of the transformed $\frac{\chi}{\chi_{max}}$ and the untransformed $1-\frac{\chi}{\chi_{max}}$ fractions can be described by the following kinetic equation:

$$\frac{d\chi}{dt} = A\left(\frac{\chi}{\chi_{max}}\right)^p \left(1-\frac{\chi}{\chi_{max}}\right)^q \qquad (2)$$

where

χ_{max} asymptotic χ value
A constant dependent on χ_{max} and on the parameters *p* and *q*.

That expression leads to the well-known Hill function as a solution:

$$\frac{\chi(t)}{\chi_{max}} = \frac{t^n}{\tau^n + t^n} \qquad (3)$$

Table II a

Kinetic parameters and asymptotic values for the doubly hill function fitted for pressures of about 10 bar.

Route a				Route b			
[P]:bar [T]:K	Kinetic parameters		Asymptotic values	[P] = bar [T] = K	Kinetic parameters		Asymptotic values
$P_i = 9.5$ $T = 523$	$\tau_1 = 0.054$ $\tau_2 = 1035$	$n_1 = 1.25$ $n_2 = 0.81$	$\chi_1 = 0.128$ $\chi_2 = 0.116$	$P_i = 10$ $T = 513$	$\tau_1 = 1.32$ $\tau_2 = 18.75$	$n_1 = 0.682$ $n_2 = 1.66$	$\chi_1 = 0.372$ $\chi_2 = 0.135$
$P_i = 9.5$ $T = 543$	$\tau_1 = 0.09$ $\tau_2 = 3.19$	$n_1 = 1.08$ $n_2 = 1.22$	$\chi_1 = 0.212$ $\chi_2 = 0.035$	$P_i = 9.5$ $T = 563$	$\tau_1 = 0.353$ $\tau_2 = 0.239$	$n_1 = 0.799$ $n_2 = 3.77$	$\chi_1 = 0.457$ $\chi_2 = 0.02$
$P_i = 9.5$ $T = 563$	$\tau_1 = 0.109$ $\tau_2 = 7.955$	$n_1 = 1.32$ $n_2 = 0.87$	$\chi_1 = 0.246$ $\chi_2 = 0.036$				
$P_i = 10$ $T = 568$	$\tau_1 = 0.130$ $\tau_2 = 10.1$	$n_1 = 1.19$ $n_2 = 1.05$	$\chi_1 = 0.270$ $\chi_2 = 0.020$				

Table II b

Kinetic parameters and asymptotic values for the doubly hill function fitted for pressures of about 7.5 bar.

Route a				Route b			
[P] = bar [T] = K	Kinetic parameters		Asymptotic values	[P] = bar [T] = K	Kinetic parameters		Asymptotic values
$P_i = 7.5$ $T = 513$	$\tau_1 = 0.67$ $\tau_2 = 6.1$	$n_1 = 1.07$ $n_2 = 1.69$	$\chi_1 = 0.159$ $\chi_2 = 0.065$				
$P_i = 7.5$ $T = 533$	$\tau_1 = 0.841$ $\tau_2 = 20.0$	$n_1 = 0.81$ $n_2 = 6.8$	$\chi_1 = 0.252$ $\chi_2 = 0.003$	$P_i = 7.5$ $T = 513$	$\tau_1 = 1.30$ $\tau_2 = 18.0$	$n_1 = 0.873$ $n_2 = 1.115$	$\chi_1 = 0.239$ $\chi_2 = 0.231$
$P_i = 7.5$ $T = 563$	$\tau_1 = 0.167$ $\tau_2 = 9.4$	$n_1 = 1.20$ $n_2 = 1.77$	$\chi_1 = 0.262$ $\chi_2 = 0.013$	$P_i = 7.5$ $T = 563$	$\tau_1 = 2.04$ $\tau_2 = 0.37$	$n_1 = 0.88$ $n_2 = 1.13$	$\chi_1 = 0.31$ $\chi_2 = 0.15$

where

$$n = \frac{2}{q-p}$$

and

$$p + q = 2$$

With τ: time to achieve the half uptake state, called characteristics time

Then, $A = \frac{n}{\tau} \chi_{max}$

When $n > 1$, the curves show an inflexion point generally associated with a nucleation process.

While a single Hill function fitted the kinetic desorption curves relatively well, in the case of absorption curves good fits require the use of a composite Hill function (Eq. (1)) under the constraint $\chi_1 + \chi_2 = \chi_{max}$.

In Figs. 9 and 10, some of the fits performed to the kinetic curves are shown.

At high temperatures, one component becomes dominant as if just one process were accounting for the kinetics. At low temperatures instead, both components have similar intensities and both processes became relevant. The fitted values are summarized in Tables II a and b.

At pressures about 10 bar—high enough above the equilibrium pressure—the difference between the kinetic parameters τ from each component depends on the temperature, changing by one order of magnitude. Although the powder consists of a heterogeneous particle size distribution, the kinetic constant shows a well-defined behavior with temperature in the case of route a, in which one of the components keeps its characteristic time τ_1 practically constant compared with the other τ_2, which becomes greater with increasing temperature.

The asymptotic values χ_1 and χ_2 of the components also change when T is increased, and the majority component dominates the whole process. Such behavior is less marked at lower pressure.

On the other hand, in all cases, there exists a nucleation process ($n > 1$) associated at least with one component. The nucleation behavior is different for each component and route. At higher temperatures, for the specimen fabricated by route a, the nucleation process is associated with the majority component, while it is associated with the minority component in the case of route b. This evidence that the route b favors the processes which don't require nucleation.

5. Conclusions

The MgH_2—TiH_2 systems result in a heterogeneous fine dispersion powder that is able to absorb hydrogen from 240 °C at pressures from 3 bar. A compromise between capacity and kinetics has been already observed and we found that the best kinetics was achieved at around 10 bar.

The kinetics of absorption agrees very well with the proposed double Hill function that takes into account two distinguishable processes, with and without nucleation. The first one may be related to surface absorption and the second tentatively ascribed to reactions at grain boundaries, dislocations and other extended defects. Both milling methods lead to similar microstructures; however, route b produces a specimen with kinetics that decreases more markedly with temperature but has a greater capacity for hydrogenation. The minor substitution of Mg in the TiH_2 phase, responsible for the change in TiH_2 cell size, does not suffice to explain the change in the sorption properties.

Substitutional Mg in the TiH_2 phase in samples of route a could lead to a more distorted state of TiH_2, responsible for better kinetics than in samples of route b [40]

Finally, we conclude that the proposed double Hill function was able to fit the whole set of absorption kinetic curves for all temperatures and fabrication routes. Moreover, the parameters reflect the different behavior of the kinetic curves obtained by such different ways.

References

[1] V. Bérubé, G. Radtke, M. Dresselhaus, G. Chen, Size effects on the hydrogen storage properties of nanostructured metal hydrides: a review, Int. J. Energy Res. 31 (2007) 637–663.

[2] P.E. de Jongh, P. Adelhelm, Nanosizing and nanoconfinement: new strategies towards meeting hydrogen storage goals, ChemSusChem 3 (2010) 1332–1348.

[3] J.F. Pelletier, J. Huot, M. Sutton, R. Schulz, A.R. Sandy, L.B. Lurio, S.G.J. Mochrie, Hydrogen desorption mechanism in MgH_2—Nb nanocomposites, Phys. Rev. B 63 (2001) 052103.

[4] H.G. Schimmel, J. Huot, L.C. Chapon, F.D. Tichelaar, F.M. Mulder, Hydrogen cycling of niobium and vanadium catalyzed nanostructured magnesium, J. Am. Chem. Soc. 127 (2005) 14348–14354.

[5] J. Charbonnier, P. de Rango, D. Fruchart, S. Miraglia, N. Skryabina, J. Huot, B. Haubackd, M. Pittd, S. Rivoirardb, Structural analysis of activated Mg(Nb)H2, J. Alloys Compd. 404–406 (2005) 541–544.

[6] G. Liang, J. Huot, S. Boily, A. Van Neste, R. Schulz, Hydrogen storage properties of the mechanically milled MgH₂–V nanocomposite, J. Alloys Compd. 291 (1999) 295–299.

[7] A. Remhof, A. Borgschulte, Thin-film metal hydrides, ChemPhysChem 9 (2008) 2440–2455.

[8] R.L. Holtz, M.A. Imam, Hydrogen storage characteristics of ball-milled magnesium-nickel and magnesium-iron alloys, J. Mater. Sci. 34 (1999) 2655–2663.

[9] P. Vermeulen, P.C.J. Graat, P.H.L. Notten, Crystal structures of MgyTi100 − y thin film alloys in the as-deposited and hydrogenated state, Int. J. Hydrog. Energy 33 (2008) 5646–5650.

[10] D.M. Borsa, R. Gremaud, A. Baldi, H. Schreuders, J.H. Rector, B. Kooi, Vermeulen, P.H.L. Notten, B. Dam, R. Griessen, Structural, optical, and electrical properties of MgyTi1 − yHx thin films, Phys. Rev. B 75 (2007) 205408.

[11] G. Liang, R. Schulz, Synthesis of Mg–Ti alloy by mechanical alloying, J. Mater. Sci. 38 (2003) 1179–1184.

[12] K. Asano, H. Enoki, E. Akiba, Synthesis of HCP, FCC and BCC structure alloys in the Mg–Ti binary system by means of ball milling, J. Alloys Compd. 480 (2009) 558–563.

[13] A. Anastasopol, T.V. Pfeiffer, J. Middelkoop, U. Lafont, R.J. Canales-Perez, A. Schmidt-Ott, F.M. Mulder, S.W.H. Eijt, Reduced enthalpy of metal hydride formation for Mg–Ti nanocomposites produced by spark discharge generation, J. Am. Chem. Soc. 135 (2013) 7891–7900.

[14] Y.J. Choi, J. Lu, H.Y. Sohn, Z.Z. Fang, Hydrogen storage properties of the Mg–Ti–H system prepared by high-energy-high-pressure reactive milling, J. Power Sources 180 (2008) 491–497.

[15] J. Lu, Y.J. Choi, Z.Z. Fang, H.Y. Sohn, E. Ronnebro, Hydrogen storage properties of nanosized MgH₂–0.1TiH2 prepared by ultrahigh-energy-high-pressure milling, J. Am. Chem. Soc. 131 (2009) 15843–15852.

[16] H. Shao, M. Felderhoff, F. Schüth, Hydrogen storage properties of nanostructured MgH₂/TiH₂ composite prepared by ball milling under high hydrogen pressure, Int. J. Hydrog. Energy 36 (2011) 10828–10833.

[17] F. Cuevas, D. Korablov, M. Latroche, Synthesis, structural and hydrogenation properties of Mg-rich MgH₂–TiH₂ nanocomposites prepared by reactive ball milling under hydrogen gas, Phys. Chem. Chem. Phys. 14 (2012) 1200.

[18] M. Ponthieu, M. Calizzi, L. Pasquini, J.F. Fernández, F. Cuevas, Synthesis by reactive ball milling and cycling properties of MgH₂–TiH₂ nanocomposites: kinetics and isotopic effects, Int. J. Hydrog. Energy 39 (2014) 9918–9923.

[19] A. Biasetti, M. Meyer, L.M. Zélis, Formation kinetics and microstructure of Mg–Ti hydrides made by reactive ball milling, Int. J. Hydrog. Energy 39 (2014) 8767–8771.

[20] F. Cuevas, D. Korablov, M. Latroche, Synthesis, structural and hydrogenation properties of Mg-rich MgH₂–TiH₂ nanocomposites prepared by reactive ball milling under hydrogen gas, Phys. Chem. Chem. Phys. 14 (2012) 1200–1211.

[21] G. Çakmak, Z. Károly, I. Mohai, T. Öztürk, J. Szépvölgyi, The processing of Mg–Ti for hydrogen storage; mechanical milling and plasma synthesis, Int. J. Hydrog. Energy 35 (2010) 10412–10418.

[22] US Department of Energy, Targets for Onboard Hydrogen Storage Systems for Light-Duty Vehicles, 2016 (accessed 10.03.16).

[23] K. Nogita, X.Q. Tran, T. Yamamoto, E. Tanaka, S.D. McDonald, C.M. Gourlay, K. Yasuda, S. Matsumura, Evidence of the hydrogen release mechanism in bulk MgH₂, Sci. Rep. 5 (2015) 8450.

[24] N. Gérard, S. Ono, in: L. Schlapbach (Ed.), Topics in Applied Physics, Hydrogen in Intermetallic Compounds I, E-Springer-Verlag, Berlin 1992, pp. 165–181.

[25] J.F. Fernández, C.R. Sánchez, Rate determining step in the absorption and desorption of hydrogen by magnesium, J. Alloys Compd. 340 (2002) 189–198.

[26] J. Haber, The role of surfaces in the reactivity of solids, Pure Appl. Chem. 56 (1984) (1663–648).

[27] P.S. Rudman, Hydriding and dehydriding kinetics, J. Less-Common Met. 89 (1983) 93–110.

[28] S. Goutelle, M. Maurin, F. Rougier, X. Barbaut, L. Bourguignon, M. Ducher, P. Maire, The Hill equation: a review of its capabilities in pharmacological modelling, Fundam. Clin. Pharmacol. 22 (2008) 633–648.

[29] R. Checchetto, G. Trettel, A. Miotello, Sievert-type apparatus for the study of hydrogen storage in solids, Meas. Sci. Technol. 15 (2003) 127–130.

[30] A.J. Lachawiec, T.R. DiRaimondo, R.T. Yang, A robust volumetric apparatus and method for measuring high pressure hydrogen storage properties of nanostructured materials, Rev. Sci. Instrum. 79 (2008) 063906.

[31] M. Meyer, L. Mendoza-Zélis, Hydrogen sorption properties of mechanically alloyed Mg1 − 2xFexTix powder mixtures, J. Alloys Compd. 611 (2014) 11–18.

[32] FullProf Suite, Crystallografic tools for Rietveld, profile matching & integrated intensity refinements of X-ray and/or neutron data, https://www.ill.eu/sites/fullprof/php/downloads.html2016 (accessed 10.03.16).

[33] A. Zaluska, L. Zaluski, J. Ström–Olsen, Nanocrystalline magnesium for hydrogen storage, J. Alloys Compd. 288 (1999) 217–225.

[34] I.P. Jain, C. Lal, A. Jain, Hydrogen storage in Mg: a most promising material, Int. J. Hydrog. Energy 35 (2010) 5133–5144.

[35] B. Vigeholm, K. Jensen, B. Larsen, A.S. Pedersen, Elements of hydride formation mechanisms in nearly spherical magnesium powder particles, J. Less-Common Met. 131 (1987) 133–141.

[36] P. de Rango, A. Chaise, J. Charbonnier, D. Fruchart, M. Jehan, P. Marty, S. Miraglia, S. Rivoirard, N. Skryabina, Nanostructured magnesium hydride for pilot tank development, J. Alloys Compd. 446–447 (2007) 52–57.

[37] A. Reiser, B. Bogdanović, K. Schlichte, The application of Mg-based metal-hydrides as heat energy storage systems, Int. J. Hydrog. Energy 25 (2000) 425–430.

[38] J. Bobet, E. Akiba, Y. Nakamura, B. Darriet, Study of Mg–M (M═ Co, Ni and Fe) mixture elaborated by reactive mechanical alloying–hydrogen sorption properties, Int. J. Hydrog. Energy 25 (2000) 987–996.

[39] H.-Y. Tien, M. Tanniru, C.-Y. Wu, F. Ebrahimi, Effect of hydride nucleation rate on the hydrogen capacity of Mg, Int. J. Hydrog. Energy 34 (2009) 6343–6349.

[40] Y. Fukai, in: R. Hull, R.M. Osgood Jr., J. Parisi, H. Warlimont (Eds.), The Metal Hydrogen System, Basic Bulk Properties, E-Springer, Berlin 2005, pp. 312–343.